JOURNAL OF GEOPHYSICAL RESEARCH, VOL. 106, NO. D24, PAGES 33,935–33,950, DECEMBER 27, 2001

Greenland snow accumulation estimates from satellite radar scatterometer data

Mark R. Drinkwater
Earth Sciences Division, European Space Agency, Noordwijk, Netherlands

David G. Long
Microwave Earth Remote Sensing Laboratory, Brigham Young University, Provo, Utah

Andrew W. Bingham
Jet Propulsion Laboratory, California Institute of Technology, Pasadena, California

Abstract. Data collected by the C band ERS-2 wind scatterometer (EScat), the Ku band ADEOS-1 NASA scatterometer (NSCAT), and the Ku band SeaWinds on QuikScat (QSCAT) satellite instruments are used to illustrate spatiotemporal variability in snow accumulation on the Greenland ice sheet. Microwave radar backscatter images of Greenland are derived using the scatterometer image reconstruction (SIR) method at 3-day intervals over the periods 1991–1998 and 1996–1997 for EScat and NSCAT, respectively. The backscatter coefficient σ° normalized to 40° incidence, A, and gradient in backscatter, B, in the range 20°–60° are compared with historical snow accumulation data and recent measurements made in the Program for Arctic Regional Climate Assessment (PARCA) shallow snow pits. Empirical relationships derived from these comparisons reveal different exponential relationships between C and Ku band A values and dry snow zone mean annual accumulation, Q. Frequency difference images between overlapping scatterometer images suggest that C band data are more sensitive to snow layering and buried inhomogeneities, whereas Ku band data are more sensitive to volume scattering from recently accumulated snow. Direct comparisons between NSCAT B values and in situ Q measurements show a linear relationship between ln (Q) and B, with a negative rank correlation of $R = -0.8$. The root-mean-square residual in fitting regression line equation $\ln(Q) = 3.08 - 17.83B$ to the data is 0.05-m snow water equivalent. This simple Ku band empirical relationship is exploited to investigate decadal changes in dry snow zone accumulation between Seasat (1978) and NSCAT (1996). Additional comparisons between NSCAT and recent QSCAT (1999) data reveal significant upslope shifts in the dry snow line along the southwestern flank of the ice sheet. Recent acceleration in the increase in intensity of scattering is observed in the percolation zone, suggesting increased melting between 2000- and 3000-m elevation in the southern half of the ice sheet.

1. Introduction

One of the most intriguing paradoxes and unanswered high-latitude earth sciences related questions is whether CO_2 doubling and accompanying global change will result in an increase (or decrease) in poleward moisture flux and an increase (or decrease) in net snow accumulation on the polar ice caps. The net mass balance of the Greenland ice cap experiences changes in response to interannual variability in snow accumulation and seasonal melting [*Appenzeller et al*., 1998; *Mote and Anderson*, 1995; *Abdalati and Steffen*, 1997]. The net mass balance is particularly sensitive to the varying climate of the Arctic region and the frequency of cyclones delivering warm moist air and precipitation to the ice sheet [*Barlow et al*., 1997]. Therefore debate continues over whether in the global warming scenario, gross accumulation increases will offset increased melting and mass loss around the coastal peripheries of the ice sheets. Indeed, as *Cuffey and Clow* [1997] suggested, there is no historical basis for expecting such a trend.

The Program for Arctic Regional Climate Assessment (PARCA) was set up in 1995 to study the regional climate processes contributing to changes in the mass balance of the Greenland ice sheet. This program has contributed significantly in recent years to our understanding of the short-term response of Greenland to ablation and accumulation. Furthermore, it has pointed to clear differences in rates of change between the interior and exterior portions of the ice sheet. Mass balance estimates are dependent on accumulation information and, more importantly, on details of its spatial variability. Recent estimates by *Thomas et al*. [2000] from PARCA transects appear to suggest that on the 1000-km scale the surface of the west Greenland ice sheet may experience thickening and thinning between extremes of -0.29 and $+0.21$ m yr^{-1}. Many of the uncertainties in net mass balance are derived from the relative uncertainty in estimates of accumulation.

Knowledge of the spatial variation in accumulation rate on

Paper number 2001JD900107.
0148-0227/01/2001JD900107$09.00

the Greenland ice sheet is derived from long-term historical in situ snow pit data reported by a number of researchers [e.g., *Benson*, 1962] and compiled by *Ohmura and Reeh* [1991]. Contemporary in situ data from shallow core sites and snow pits during PARCA are used to augment these data. Together, these contribute to a spatially interpolated picture of the mean annual snow accumulation rate, albeit from a variety of time spans and years in each location. Recent PARCA accumulation measurements, though providing some contemporary point estimates, do not augment the spatial or temporal detail to the point necessary to be able to estimate regional interannual variations in mass balance. Associated covariability in snow physical characteristics implies spatial variability in the microwave penetration depth. This makes interpretation of recent Ku band satellite altimeter topographic change estimates difficult [*Davis et al*., 1998, 2000; *Zwally and Brenner*, 1989].

Satellite-borne microwave sensors are well suited to making frequent measurements of the Greenland ice sheet. With year-round, day-night, and all-weather imaging capability they provide a unique perspective on spatial and temporal variability in surface properties. *Zwally* [1977], *Comiso et al*. [1982], and *Zwally and Giovinetto* [1995] applied passive microwave radiometer data in estimates of grain size and accumulation on the Antarctic ice sheet. Their technique is restricted somewhat by the limited time of day sampling or coarse resolution offered by these data as well as by the fact that currently available high-frequency radiometer data provide little direct information on snow emission characteristics deeper than the top few centimeters of snow. Active microwave radar currently provides us with high (25 m) spatial resolution information on characteristics of the Greenland ice sheet [*Fahnestock et al*., 1993] and its shape and dynamic response in the form of interferometric fringes from synthetic aperture radar (SAR) image pairs [*Joughin et al*., 1995]. The major limitation on use of SAR has traditionally been the large volume of data involved, together with the fact that there is a trade-off between generation of large-area, high spatial resolution mosaics and temporal resolution. *Forster et al*. [1999] recently used the *Fahnstock et al*. [1993] Greenland ERS-1 SAR mosaic with some success but discovered that swath-to-swath variability and the incidence angle of these data make snow accumulation interpretation difficult. At low SAR incidence angles (20°–23°), surface roughness contributes significantly to the backscatter [*Jezek et al*., 1993]. Ideally, for snow accumulation estimates, higher incidence angle, higher-frequency data are required so that the penetration depth limits the scattering response to the upper units of accumulated snow. The sensitivity of the backscatter coefficient (at higher incidence angles exceeding 40°) to snow accumulation only becomes significant at the point where the wavelength scale relative to the typical grain size is short enough for the scattering component of extinction to dominate. For a typical polar snowpack with mean grain radii on the order of ~0.5 mm the frequency must exceed 5 GHz before the scattering albedo k_s/k_e (i.e., the ratio between the scattering coefficient k_s and extinction coefficient k_e) exceeds 0.1. Ku band provides a balance between penetration and snow grain scattering.

Over the last several years a new Greenland radar image data set has been compiled from a variety of radar scatterometer missions. Enhanced resolution images from the 13.6 GHz (Ku band) Seasat A scatterometer system (SASS) [*Long and Drinkwater*, 1994], the 5.3 GHz (C band) ERS-1 and ERS-2 scatterometer [*Drinkwater and Long*, 1998], and the 13.6 GHz (Ku band) NASA scatterometer (NSCAT) [*Long and Drinkwater*, 1999] have been applied to studies of the Greenland and Antarctic ice sheets. *Long and Drinkwater* [1994] first reported an inverse correlation between Ku band backscatter values and snow accumulation. More recently, P. Gudmandsen and N. Kruopis (personal communication, 1998), *Wismann and Boehnke* [1997], and *Kruopis* [1999] investigated this relationship in further detail using C band ERS-1 and ERS-2 scatterometer data.

In this paper we exploit simple relationships between backscatter and the physical properties of the layered firn to make snow accumulation rate estimates. In section 2 we demonstrate how combinations of simultaneous C and Ku band data from different satellites can be exploited to define Greenland snow and ice facies. In section 3 these results facilitate a comparison of dry snow zone scatterometer and historical in situ snow accumulation data, and simple empirical relationships between backscatter and snow accumulation are derived. Section 4 describes a simple layered electromagnetic scattering model that may be used to establish the physical basis for observed empirical relationships. Section 5 shows results of validating the spatial distribution of snow accumulation estimates made using the empirical relationships. In section 6, accumulation estimates made using different Ku band data are compared, and conclusions are drawn about spatial variability and changes in Greenland snow accumulation during the satellite era.

2. Ice Sheet Applications of Scatterometer Image Data

Cryospheric applications of wind scatterometer image data have matured significantly since *Drinkwater and Long* [1993] produced the first ERS-1 full polar images and *Long and Drinkwater* [1994] demonstrated the capability for characterizing snow and ice facies on the Greenland ice sheet using SASS data. More recently, *Drinkwater and Long* [1998] and *Long and Drinkwater* [1999] exploited Ku band NSCAT data in conjunction with SASS and ERS-1/2 wind scatterometer (hereinafter EScat) data for studying melt extent and seasonal to interannual changes on the surface of Greenland and Antarctica. These applications have been extended with interpretations of Antarctic EScat backscatter anomaly time series [*Bingham and Drinkwater*, 2000] and by retrievals of streamlines of surface inversion winds through a relationship between backscattering anisotropy and aligned snow surface roughness features [*Long and Drinkwater*, 2000]. In this section we focus on the multiple scatterometer data sets assembled specifically for studying changes in the Greenland ice sheet and investigate the applicability of this long-term radar backscatter record for characterizing seasonal to interannual changes.

2.1. Scatterometer Data Sets

Scatterometers such as SASS, EScat, NSCAT, and SeaWinds were originally designed to measure the surface backscatter of the ocean in order to estimate the near-surface wind speed [*Naderi et al*., 1991]. Thus their application to cryosphere studies is a serendipitous example of the interdisciplinary nature of microwave remote sensing. A description of these sensors is briefly given below (see "Special Issue on Emerging Scatterometer Applications," in *IEEE Transactions on Geoscience Electronics*, *38*(4), 2000, for further information).

The Ku band SASS flew for 100 days in 1978, from July

through early October. SASS demonstrated the utility of scatterometer data primarily for ocean wind measurements. It also collected data over land and is the oldest available microwave radar data set. SASS data are thus crucial in studies of global change. SASS collected both vertical transmit and receive polarization (VV) and horizontal transmit and receive polarization (HH) data, though most data collected over ice were VV. The nominal measurement resolution was 50 km with measurements collected over a broad (0°–70°) incidence angle range on an irregular grid at two azimuth angles on each side of a dual-sided 500-km-wide swath.

The EScat mode of the European Remote Sensing (ERS) Active Microwave Instrument (AMI) collects C band VV. A series of two satellites have been collecting scatterometer data continuously since 1992. Data are acquired over a single 500-km-wide swath at a nominal resolution of 50 km on a 25-km regular grid. Since the SAR and scatterometer modes of the AMI are mutually exclusive, gaps in the EScat data occur during SAR mode data collection. EScat resolution is determined primarily by spatial filtering applied during ground processing of the signal.

The NSCAT was a follow-on mission to SASS. It operated from September 1996 through June 1997. Like SASS, NSCAT data collection ended prematurely due to a spacecraft power system failure. NSCAT collected 25-km backscatter measurements over two 600-km-wide swaths at both VV and HH. Backscatter is measured at 10° and 16°–62° incidence angles at three azimuth angles on a regular 25-km grid. Like SASS, NSCAT used antenna pattern, Doppler filtering, and measurement timing to achieve spatial resolution.

In June 1999 the SeaWinds on QuikScat (QSCAT) scatterometer was launched and is presently operating. This Ku band scatterometer is based on a rotating pencil-beam antenna which provides a much wider, more continuous swath than previous scatterometers. A second SeaWinds is scheduled for launch aboard ADEOS-II in late 2001. While the fundamental resolution is set by the antenna footprint size, onboard signal processing improves the resolution to 6×25 km [*Spencer et al*., 1997, 2000]. Unlike previous instruments, QSCAT makes backscatter measurements at only a single incidence angle per polarization: 46° for HH and 54° for VV. The wide swath enables complete single-day coverage of the polar regions in contrast to the other sensors which require multiple days for complete polar coverage.

Backscatter measurements from these scatterometers were used in the scatterometer image reconstruction (SIR) resolution enhancement algorithm [*Long et al*., 1993] to generate images of the surface backscatter characteristics. Images are made by combining data from multiple passes over the study site. The SIR algorithm takes advantage of the spatial overlap and response function of the measurements to generate enhanced resolution images of the backscatter A (in dB) normalized to 40° incidence and the slope B of the backscatter versus incidence angle (in dB deg^{-1}). These are related to the measured backscatter of the target via the relationship

$$\sigma^\circ(\theta) = A + B(\theta - 40). \quad (1)$$

Differences in spatiotemporal sampling and response functions of each instrument yield differences in the effective resolutions of the images. The effective resolution is also a function of the number of passes included in the data. Thus there is a trade-off between spatial and temporal resolution and noise in the resulting image data [*Drinkwater and Long*, 1993; *Long and Drinkwater*, 1994]. Enhancing the resolution tends to increase the noise. However, the signal-to-noise ratio of these scatterometer measurements is large, and for this study this noise component is negligible. In this study, SASS images are generated using 2 weeks of data at weekly intervals, while NSCAT and EScat images are generated with 6 days of data at 3-day intervals. By way of its greater coverage, QSCAT A images are generated with a single day's worth of data. As a result, SASS and NSCAT images have a pixel spacing of 4.45 km and an effective resolution of ~8–10 km, while a pixel spacing of 8.9 km is used for EScat, yielding an effective resolution of ~20–25 km for most areas. QSCAT images, in contrast, have pixel spacings of either 2.225 or 4.45 km with effective resolutions of either ~5–8 km or ~8–10 km, respectively [*Spencer et al*., 2000]. The key purpose of the SIR algorithm in this study is to produce images of A and B.

2.2. Mapping Snow and Ice Facies

Long and Drinkwater [1994, 1999] found Ku band and C band scatterometer data to be extremely effective for delimiting snow and ice facies because of the sensitivity of microwaves to the physical characteristics of the snow and firn in the top few meters. This result is consistent with the findings of *Rott* [1980], *Thomas et al*. [1985], *Mätzler* [1987], *Jezek et al*. [1994], and *Wismann and Boehnke* [1996]. Here we demonstrate how the combined data sets can be exploited to define and extract snow facies information.

Plate 1 shows a composite of the data sets used in this study. SASS image data are limited by the orbit inclination of 78.5°N. The only period of common seasonal data among all of the satellite records is late autumn, during September and early October. The most dramatic variability occurs in summer (typically July) microwave images as precipitation and melting occur in the percolation and ablation zones [*Long and Drinkwater*, 1999; *Wismann*, 2000] (Plate 1e). Previous melt time series clearly demonstrate that by early September the surface has cooled and frozen such that the backscatter signatures of these areas remain stable throughout the winter. In Plate 1e a frequency difference image is generated between simultaneous data acquired by NSCAT and ERS-2 during 1996. In contrast, in Plate 1c a temporal difference was generated to illustrate decadal changes taking place between 1978 SASS and 1996 NSCAT imaging periods. It was generated under the assumption that there is very little interannual variability in autumn season characteristics of the surface.

The primary features of Plate 1 indicate that summer surface melting creates diagenetic changes in the snowpack which lead to distinctive spatial variations in σ°. Refreezing of downward percolating meltwater leads to permanent buried ice lenses and ice pipes in the percolation zone, which in winter produce intense backscattering [*Long and Drinkwater*, 1994]. Plates 1a, 1b, and 1d exhibit these characteristics, with a bright red halo of σ° values close to and exceeding 0 dB in this zone. Within central Greenland the dry snow region is one of relatively lower backscatter at 40° incidence angle. At these higher elevations the surface experiences no melting, and this region experiences negligible seasonal variability in σ°. Both the extent of the relatively low backscatter central zone and the halo of intense scattering closely resemble features identified in the SAR mosaic of *Fahnestock et al*. [1993].

Because of the penetrating capability of microwaves in dry firn, the difference image in Plate 1c reveals archaeological evidence of previous melting. Buried ice lenses generated by

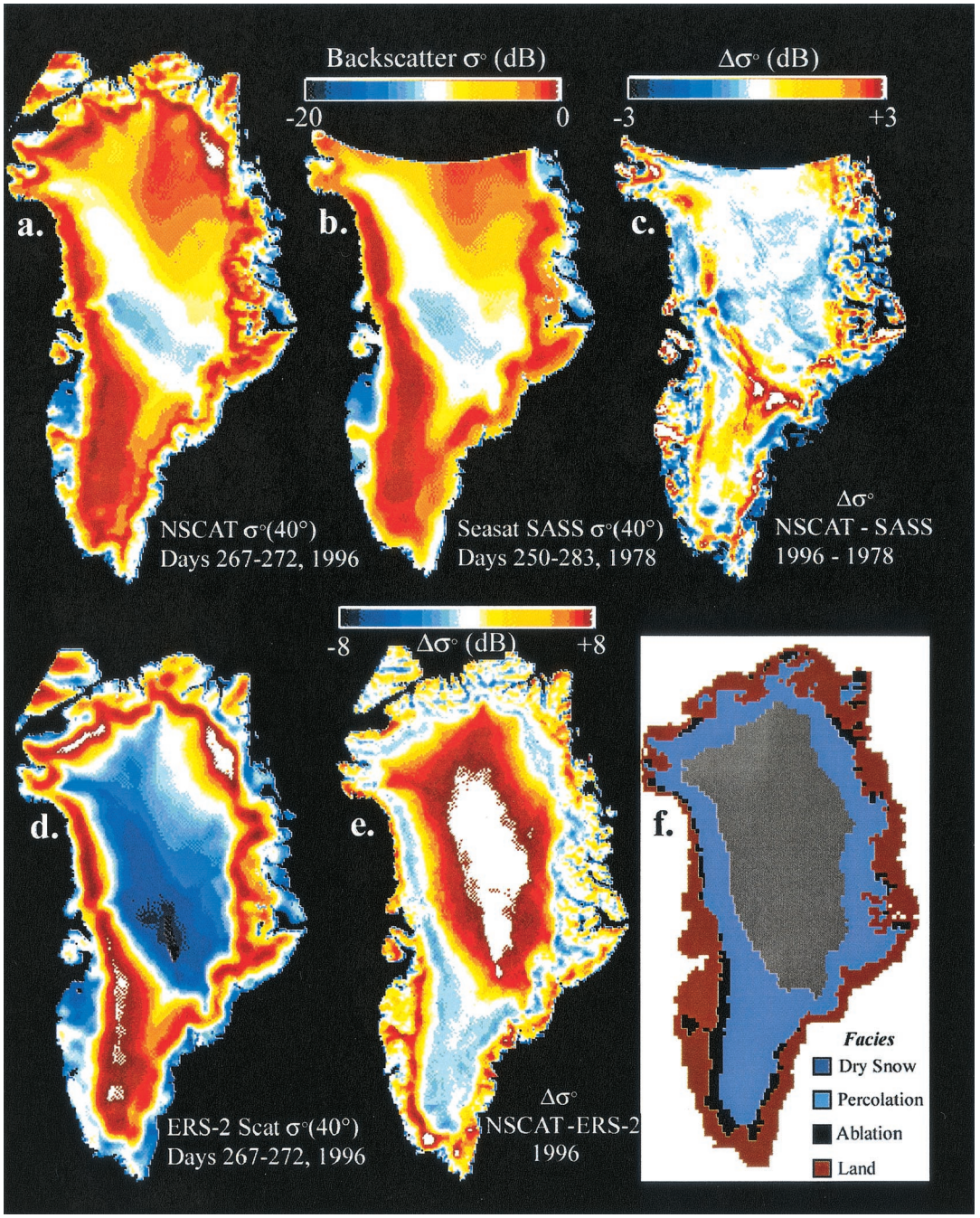

Plate 1. Greenland scatterometer images showing (a) NSCAT (Ku band) A values, (b) SASS (Ku band) A values, (c) NSCAT − SASS (Ku band) difference ΔA, (d) EScat (C band) A values, and (e) NSCAT − EScat (Ku band–C band) difference ΔA. (f) Snow facies automatically derived from Plates 1a–1e. Plates 1a and 1d use the same color scale as Plate 1b.

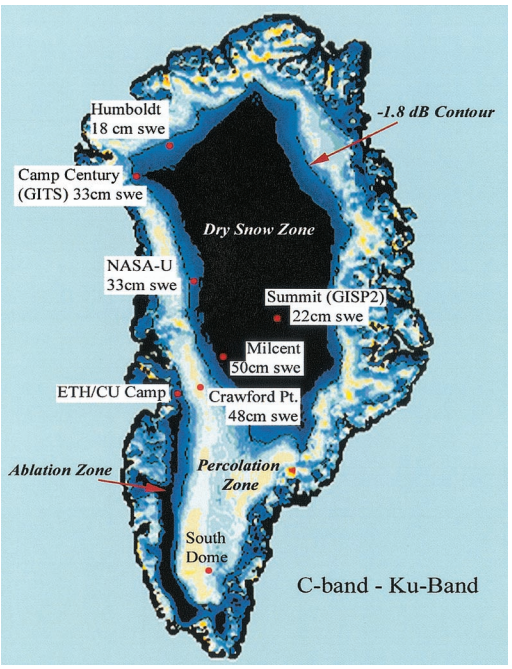

Plate 2. EScat − NSCAT (C band − Ku band) A difference image showing $\Delta A = -1.8$ dB contour used to define the lower dry snow zone boundary. PARCA in situ sites and snow accumulation values are provided.

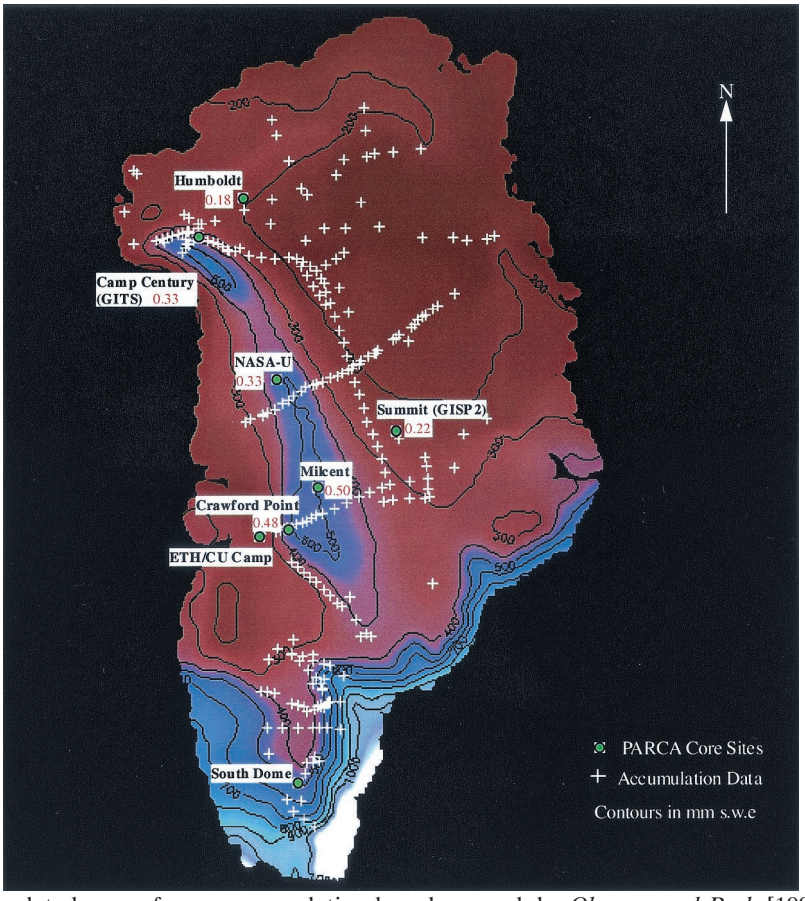

Plate 3. Interpolated map of snow accumulation based on work by *Ohmura and Reeh* [1991] and shallow core sites. PARCA field sites are indicated along with the typical annual accumulation (in meters snow-water equivalent (SWE)) at these locations.

refreezing of downward percolating meltwaters are revealed in locations where the surface experienced summer season melting. Percolation features are revealed as significant differences exceeding 3 dB or more in Plate 1c, suggesting that the melt line had ascended to higher elevations and encroached upon the lower margins of the dry snow zone between 1978 and 1996. NSCAT and SASS data therefore provide valuable yardsticks for decadal changes.

2.3. Defining the Dry Snow Zone

In Plate 1f, Ku and C band images are combined for the purpose of dry snow and percolation zone facies delimitation. The dry snow line in Plate 2 is defined by differencing EScat and NSCAT images acquired simultaneously during the time interval between days 267 and 272, 1996. A large frequency contrast in σ° is evident in the dry snow zone, with differences tending to values between 6 and 8 dB in Plate 1e. Backscatter models indicate that the snow crystal volume scattering efficiency (or single scattering albedo k_a) is much greater at Ku band than at C band in typical Greenland dry snow. The NSCAT − EScat difference (i.e., frequency contrast) in Plate 1e reverses quickly, however, in the vicinity of the dry snow line from values of +6 to −2 dB. Airborne synthetic aperture radar (AIRSAR) C, L, and P band data transects demonstrate similar frequency contrast reversals in the percolation zone [*Jezek et al*., 1993]. Results of *Jezek et al*. [1994] appear to explain the origin of the reversal, with in situ radar evidence indicating that C band penetrates deeper than Ku band in the percolation zone to sense more buried scatterers (i.e., ice lenses, ice glands, and pipes).

The simple methodology proposed here for dry snow zone definition relies on the fact that recent melting has a profound impact on C band data (and lesser effect at Ku band), resulting in strong horizontal gradients at the upper margin of buried scatterers created by percolation. In Plate 2 the −1.8-dB contour is selected arbitrarily to define the dry snow line. A negative value is chosen to ensure that the scattering albedo is greater at Ku band than at C band and that there is absolutely no effect from grain transformation or melting. Various values were tested during winter without a significant temporal shift in the location of the boundary (since the frequency difference gradient remains large throughout winter). The value of −1.8 dB is found to provide a simple yet robust quantitative microwave radar remote sensing definition for the dry snow line.

The result in Plate 2 is the contour defining the boundary between the percolation and dry snow facies. Time series C band EScat images confirm that this radar-defined dry snow line delimits the elevation above which, by definition, negligible summer season change takes place. Only a slight seasonal variation (±0.15 dB) is observed in dry snow volume scattering as a result of the seasonal temperature cycle [*Wismann*, 2000]. Thus the −1.8-dB contour is filled to produce the dry snow region image whose extent is mapped in Plate 1e. This region is used hereinafter to define which pixels and in situ data lie within the dry snow zone.

3. Relationships Between Snow Accumulation and Scatterometer Data

3.1. In Situ Characterization of Greenland Snow Accumulation

Various historical in situ data have been assembled from *Benson* [1962], *Ohmura and Reeh* [1991], and a number of recent PARCA shallow core measurements by *Bales et al*. [2001] into a spatially interpolated map of snow accumulation rate. The map in Plate 3 is generated using both the historical data compiled by *Ohmura and Reeh* [1991] from a variety of sources and the shallow core data available at the time of this study. The resultant contoured accumulation pattern is a low-pass spatially and temporally filtered data set in which the color is representative of the secular mean of accumulation estimates made in different locations during different seasons and multiyear intervals between 1952 and 1998 (and may not be completely representative of the more up-to-date PARCA accumulation maps shown elsewhere in this issue). Crosses in Plate 3 indicate the geographic locations of all the in situ input data, and additional PARCA accumulation estimates are used from the shallow core site locations in Table 1.

Table 1. Locations of Greenland Ice Core and Long-Term in Situ Snow Accumulation Records

Location	Latitude N	Longitude W	Elevation, m
Humboldt	78.53°	56.83°	1995
Camp Century (GITS)	77.14°	61.04°	1887
NASA-U	73.84°	49.49°	2369
Summit	72.58°	38.50°	3254
Milcent	71.00°	45.00°	2500
Crawford Point	69.88°	46.99°	2022
ETH/CU Camp	69.57°	49.32°	1149
South Dome	63.15°	44.82°	2922

Most of the recent PARCA accumulation rate estimates are representative of the overall picture provided by the colorized and contoured data, except for the NASA-U site, where no local data were incorporated into the interpolated map. The ice sheet exerts a strong topographic control on precipitation with generally relatively less precipitation to the east of the crestline of the ice sheet, except southeastern Greenland, where accumulation rates are highest. North central and northeast Greenland have the least accurate picture of accumulation, but limited in situ data indicate the lowest accumulation rates in this region.

3.2. Scatterometer Versus in Situ Data

Comparisons were made between individual *Ohmura and Reeh* [1991] and PARCA accumulation estimates and single-pixel scatterometer A and B values in EScat and NSCAT images (at the geographic locations marked by crosses in Plate 3). Little relationship appears to exist in Figure 1a between C band A values and snow accumulation Q in mm snow-water equivalent (SWE), whereas C band B values in Figure 1b exhibit a reasonably strong exponential relationship. The relationship defined by the least squares fit dotted curve,

$$\ln(Q) = 2.86 - 16.01B, \tag{2}$$

has a residual error standard deviation of 0.071 m SWE and a correlation coefficient of $R = -0.7675$. This exponential relationship is similar to one observed by P. Gudmandsen and N. Kruopis (personal communication, 1998) using EScat data from the April–May 1993 period.

In contrast to C band, dry snow NSCAT Ku band A values appear to display a more direct relationship with Q (see Figure 1c), with a correlation of $R = -0.65$. Percolation zone points separate in this case as a distinct cluster of points on the right side of Figure 1c. This implies that old percolation features

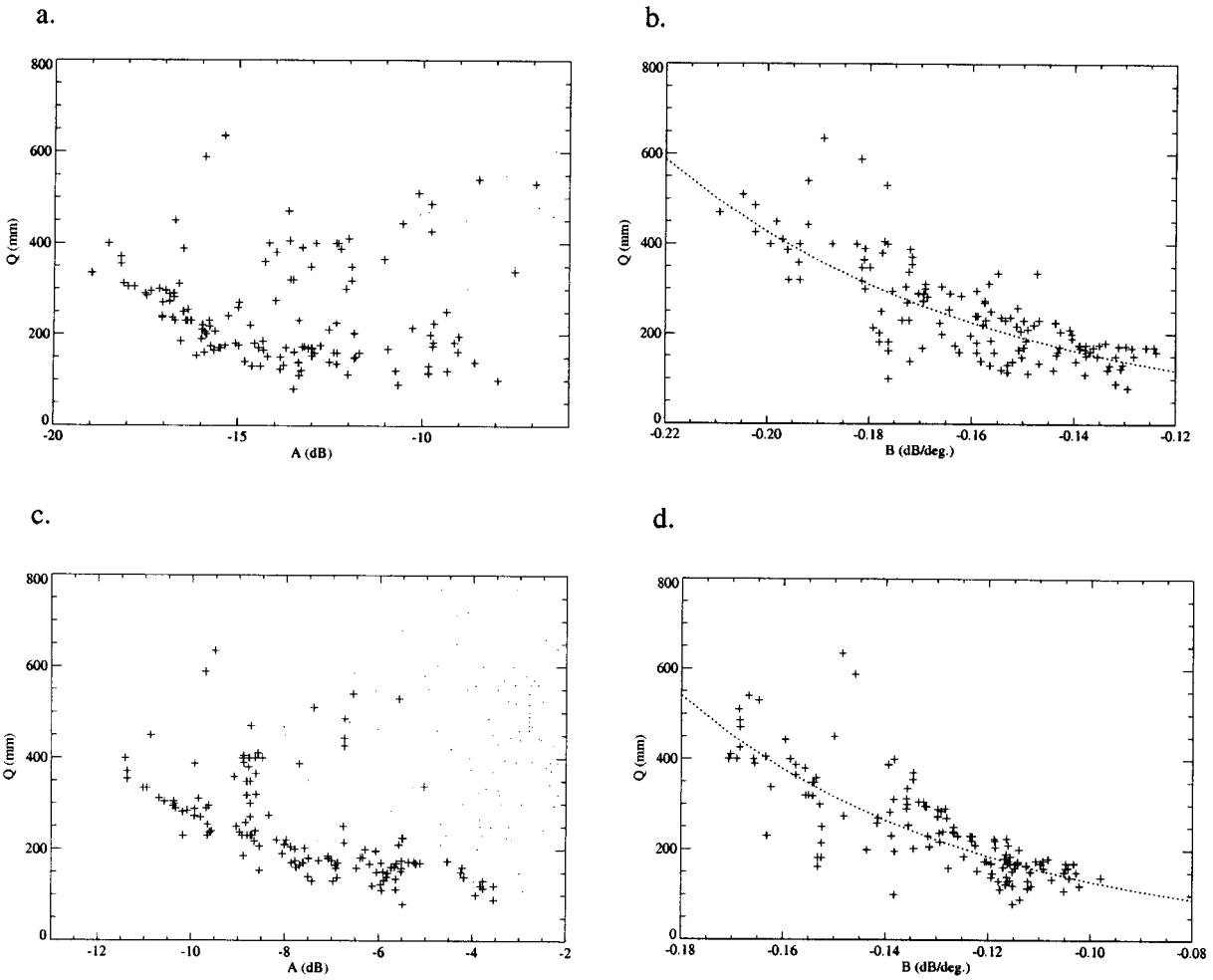

Figure 1. Comparison of scatterometer image pixel values with in situ accumulation data Q (in mm SWE) for (a) EScat A data, (b) EScat B data, (c) NSCAT A data, and (d) NSCAT B data from days 263 to 272, 1996. Dotted curves in Figures 1b and 1d indicate least squares fit to the B data. In situ measurement locations within the dry snow zone are represented by crosses, whereas those outside the dry snow zone (presumed to experience melt) are shown as small dots.

buried below several years of recent dry snow accumulation (particularly around the fringes of the dry snow zone) are less likely to have an impact on Ku band dry snow volume scattering.

NSCAT B data in Figure 1d show a fairly similar exponential relationship to that in Figure 1b with the least squares fitted curve,

$$\ln (Q) = 3.08 - 17.83B, \tag{3}$$

and a slightly improved correlation coefficient of $R = -0.81$. This exponential fit results in a smaller bias and a smaller residual error standard deviation of 0.066 m SWE.

For raw independent scatterometer measurements, absolute and relative calibration accuracies of ±0.5 dB and ±0.15 dB, respectively [*Long and Skouson*, 1996], imply a similar accuracy in the average SIR A image pixel results presented here. The B estimation accuracy is of the order of ±0.05 dB deg^{-1}. Unfortunately, no measurement accuracy figures are provided by *Ohmura and Reeh* [1991]. This makes it difficult to assess the significance of a small overall improvement in explained variance from 56 to 66% between C and Ku band B results in Figure 1. Recent PARCA shallow core snow accumulation data imply an upper limit accuracy of ~±0.05 m in estimating Q [*Anklin et al.*, 1998].

Bearing these estimated accuracies and the sensitivity of the scatterometer in mind, root-mean-square (RMS) residuals in the fitted C band relationship tend to become larger than Ku band in high A, low B value locations corresponding to regions of lower accumulation rates. Greater accuracy is required to resolve small changes in accumulation rates, particularly in the low-accumulation region in northeast Greenland where few in situ data exist. The Ku band relationship performs better in these regions, while also minimizing spurious buried percolation effects around the dry snow zone margin.

3.3. Scatterometer Versus Interpolated Data

On the basis of the relationship observed in Figure 1d a further comparison is made between scatterometer B image values and the accumulation map shown in Plate 3. Q values were interpolated to each dry snow zone pixel location to enable the maximum possible comparison of snow accumulation and scatterometer data. Data points shown in Figure 2

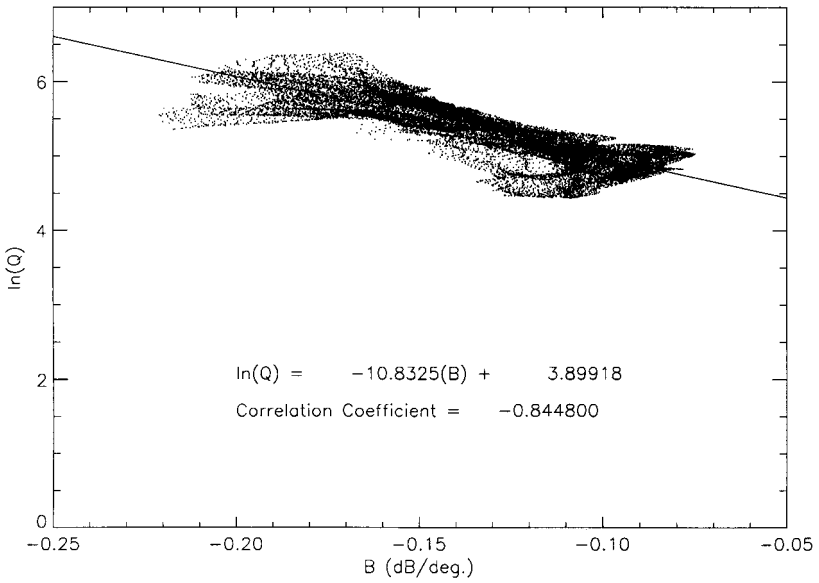

Figure 2. Scatterplot indicating the relationship between interpolated pixel snow accumulation Q values from Plate 3 and dry snow pixel B values from NSCAT. The line indicates a linear regression fit to the data, with the corresponding correlation coefficient and linear equation.

represent all B image pixels within the dry snow zone in Plate 2. A similarly strong relationship is observed between the accumulation Q and the individual pixel B values, with a correlation coefficient of $R = -0.85$. The regression in Figure 2 suggests that >72% of the variance is accounted for by the exponential relationship between B and Q. The error standard deviation computed from the regression is ~49 mm yr^{-1} SWE. The mean error is unbiased and close to 0, while the tails in the error distribution are largely controlled by the errors in the interpolated Greenland accumulation map.

Some problems are evident in Figure 2 that are caused by interpolation difficulties in locations where values are extrapolated over large distances between measurements. These are expressed as clustered lines of pixel values in regions where there are sparse in situ accumulation data. In these locations the interpolated values of Q are clearly an artifact of the interpolator and are unrepresentative of the true accumulation. This highlights the deficiencies of accumulation charts such as that derived by *Ohmura and Reeh* [1991]. RMS errors are expected to be significantly reduced when a comparison is made with the updated Greenland accumulation chart including all recent PARCA field data.

4. Simulated A and B Relationship With Accumulation

4.1. Multilayer Scattering Model

In order to understand how accumulation affects scatterometer A and B images we have developed a simple multilayer scattering model. This model is explained in greater detail by *Bingham and Drinkwater* [2000, also manuscript in preparation, 2001] and is qualitatively similar to that presented by *Forster et al*. [1999].

Snow studies in Greenland and Antarctica have shown that the snowpack or firn consists of a layered sequence [*Shuman et al*., this issue]. Layering, or stratification, results from seasonally discontinuous accumulation of snow at the surface and from changes in meteorological conditions. Microwave backscattering occurs at dielectric interfaces, such as the boundary between adjacent layers or the air-ice interface of ice grains within the volume of each layer. Our multilayer scattering model therefore consists of two components. The first component describes the physical and thermal characteristics of each of the firn layers (depth, thickness, density, grain size, and temperature). This determines the dielectric properties of each layer, the microwave penetration depth, and the extinction coefficient k_e. The second component describes the scattering mechanisms required for computing the backscattering coefficient. Further details of the model description are given by *Bingham and Drinkwater* [2000].

The method that we adopted was to compute firn layer characteristics at annual intervals. Over these intervals the physical characteristics and snow accumulation rate are assumed to remain constant. Layer depth z is given by *Bolzan*, [1985]

$$\frac{\partial z}{\partial t} = \frac{Q\rho_i}{\rho_s(z)}, \tag{4}$$

where t is the layer age, Q is the accumulation rate (expressed in meters SWE yr^{-1}), ρ_i is the density of ice (917 kg m^{-3}), and $\rho_s(z)$ is the density of the layer as a function of depth. Analytically, (4) can be solved if ρ is assumed to vary linearly with depth [*Forster et al*., 1999]. Shallow pit and ice core studies show that over C and Ku band depths of penetration (<20 m) a linear density-depth assumption is valid [*Bolzan and Stroebel*, 1994]. In this case, $\rho_s(z) = \rho_0 + dz$, where ρ_0 is the density of the surface layer and dz is the densification constant (dz = 0.01 kg m^{-3} [from *Gow*, 1968]).

A grain-size profile is computed using a simple grain-growth model based on the Arrhenius equation. This approach assumes that snow grains grow by transfer of atoms across their boundaries. The growth rate is therefore determined by the transfer rate, which is controlled by the interfacial free energy of the grain boundaries. The equation for this model is

$$r(t)^2 = r_0^2 + k_0 t e^{-(E/RT)}, \quad (5)$$

where r is the grain radius, r_0 is the initial grain radius, k_0 is the constant 6.75×10^7 mm^2 yr^{-1} [after *Alley et al*., 1982], E is the activation energy for the grain-growth process, R is the gas constant (8.314 J mol^{-1} K^{-1}), and T is the mean annual temperature. Using grain-size profiles observed in polar firn, *Gow* [1969] and *Alley et al*. [1982] have demonstrated that this function works well with $E = 42.3$ kJ mol^{-1}.

Temperature profiles were computed as an exponentially decaying sinusoid [*Paterson*, 1994]. Meteorological data for the Greenland summit show that the mean annual surface air temperature is −32°C, peak-to-peak amplitude is 15°C, and minimum air temperatures typically occur in February [*Shuman et al*., 1998].

The total backscatter σ° from an n-layer polar snowpack is computed using a radiative transfer model [*Bingham and Drinkwater*, 2000, also manuscript in preparation, 2001]:

$$\sigma^\circ = \sigma_s^\circ(\theta_0) + \Gamma_{0,1}^2(\theta_0)\sigma_{v1}^\circ(\theta_0) + \sum_{j=2}^{N} \frac{\prod_{i=1}^{i=j} \Gamma_{i-1,i}^2(\theta_{i-1})}{\prod_{i=1}^{i=j-1} L_i^2(\theta_i)} \sigma_{vj}^\circ(\theta_j), \quad (6)$$

where σ_s° and σ_v° represent surface and volume backscatter, respectively, both of which are incidence angle θ dependent. Γ is the transmissivity between adjacent layers, and L is the one-way loss factor, given by $L = \exp(dk_e \sec\theta')$, where d is layer thickness and θ' is the refracted incidence angle.

Surface scattering is assumed to occur only at the air-snow interface. This is valid because there is no significant density contrast at the annual accumulation layer interfaces, so the dielectric contrast and therefore the reflectivity at these interfaces is small. The surface backscatter component is computed using a Kirchoff surface scattering model under a scalar approximation [*Ulaby et al*., 1982; *Eom*, 1982] with an exponential surface height correlation function [*Long and Drinkwater*, 1994]. In general, surface scattering only dominates at incidence angles less than around 30°. Consequently, A values are independent of surface roughness because they are measured at 40° incidence angle, whereas B values are more strongly dependent on surface roughness because they also rely on measurements in the 20°–30° incidence angle range.

The volume scattering component for each layer is modeled using Mie scattering theory. Each layer is assumed to consist of loosely packed independent spherical scatterers (ice grains) smaller than the radiation wavelength [*Attema and Ulaby*, 1978]. Using this approach, σ_v° is strongly dependent on the cross section of scatterers and layer thickness (accumulation) and to a lesser extent, on the density of scatterers. There is also a decay with incidence angle due to a path-length-dependent loss or attenuation in the medium expressed by L. At low- to mid-incidence angles, volume scattering is relatively flat, while at higher incidence angles, backscatter rolls off due to an increase in the illumination area.

4.2. Model Simulation of A and B Values

Figure 3 shows results of simulation of Ku band backscatter values as a function of accumulation for typical layered Greenland firn using the model described in section 4.1. Figure 3a shows the age (i.e., depth) dependence of grain radius (where $r_0 = 2.5 \times 10^{-3}$ m), the density (with $\rho_0 = 360$ kg m^{-3}) prescribed in the model, and the resulting layer-age-dependent volume scattering contribution. The air-snow interface roughness is fixed with typical values of the standard deviation and correlation length of surface height of $\sigma_h = 3.5 \times 10^{-3}$ m and $l = 0.05$ m, respectively. These are typical values that have been observed for snow surfaces in the Arctic [*Bingham*, 1997]. In Figure 3b, σ° is simulated for a variety of annual mean Q values ranging between 0.10 m yr^{-1} SWE (solid line) and 0.70 m yr^{-1} SWE (long-dashed line) at intervals of 0.20 m yr^{-1}. As previously concluded by *Forster et al*. [1999], backscattering at incidence angles below 30° is dominated by snow surface scattering. The decay of σ° with incidence angle in the range $30° \le \theta \le 60°$ is characteristic of previous SASS Ku band measurements in the dry snow zone [see, e.g., *Long and Drinkwater*, 1994, Figure 10]. These curves are close to observed values.

Simulated A and B values in Figures 3c and 3d decay exponentially with increasing Q and bear a strong resemblance to the observed data in Figure 1. The reason for this decrease can be explained in terms of the increase in the layer loss factor with increasing layer thickness. This increase in loss factor reduces the number of layers penetrated by the microwave radiation. Increases in accumulation also lead to a decrease in the net size of the scattering grains. This reduces A values and introduces a steeper rate of decrease in the backscatter with incidence angle, which reduces B values.

We experimented with a number of hypothetical layered firn characteristics (similar to those employed by *Bingham and Drinkwater* [2000]) and found that the relationship between A and B and accumulation is stable but that their sensitivity varies. For example, in regions of melt-induced inhomogeneities (e.g., buried ice lenses) or layering, volume scattering is significantly enhanced. This results in high values of A but generally in less sensitivity to changes in accumulation. Similarly, for increasingly rough surfaces, B tends toward larger and larger negative gradients and becomes less sensitive to accumulation.

Though the model does not perfectly simulate the general large-scale scattering response, simulations show that σ° is sensitive to snow accumulation and SWE of layered firn over the broad incidence angle range measured by a fan-beam radar scatterometer. Dry firn is relatively transparent, and therefore σ° is strongly related to the scattering albedo k_s/k_a. Since the extinction coefficient k_{ext} regulates the penetration depth (i.e., path length) for a given incidence angle and because k_{ext} depends to a large extent on grain size (and scattering coefficient k_s) and the depth and density of the firn layer (i.e., absorption coefficient k_a), σ° (and its variation with incidence angle B) is sensitive to spatial variability in the mean SWE in the upper layers of firn. In this scheme an increased sensitivity of B to Q at higher frequency is explained by the increase in scattering albedo of the firn between Ku and C band.

5. Scatterometer-Estimated Snow Accumulation Results

5.1. Scatterometer Estimates of Snow Accumulation

Spatial estimates of dry snow zone accumulation are achieved by using the empirical relationship developed in section 3.3 and shown in Figure 2, with B values corresponding to the NSCAT image in Plate 1a. The result is shown in Plate 4. Rather than mask around the lower elevation boundary of the

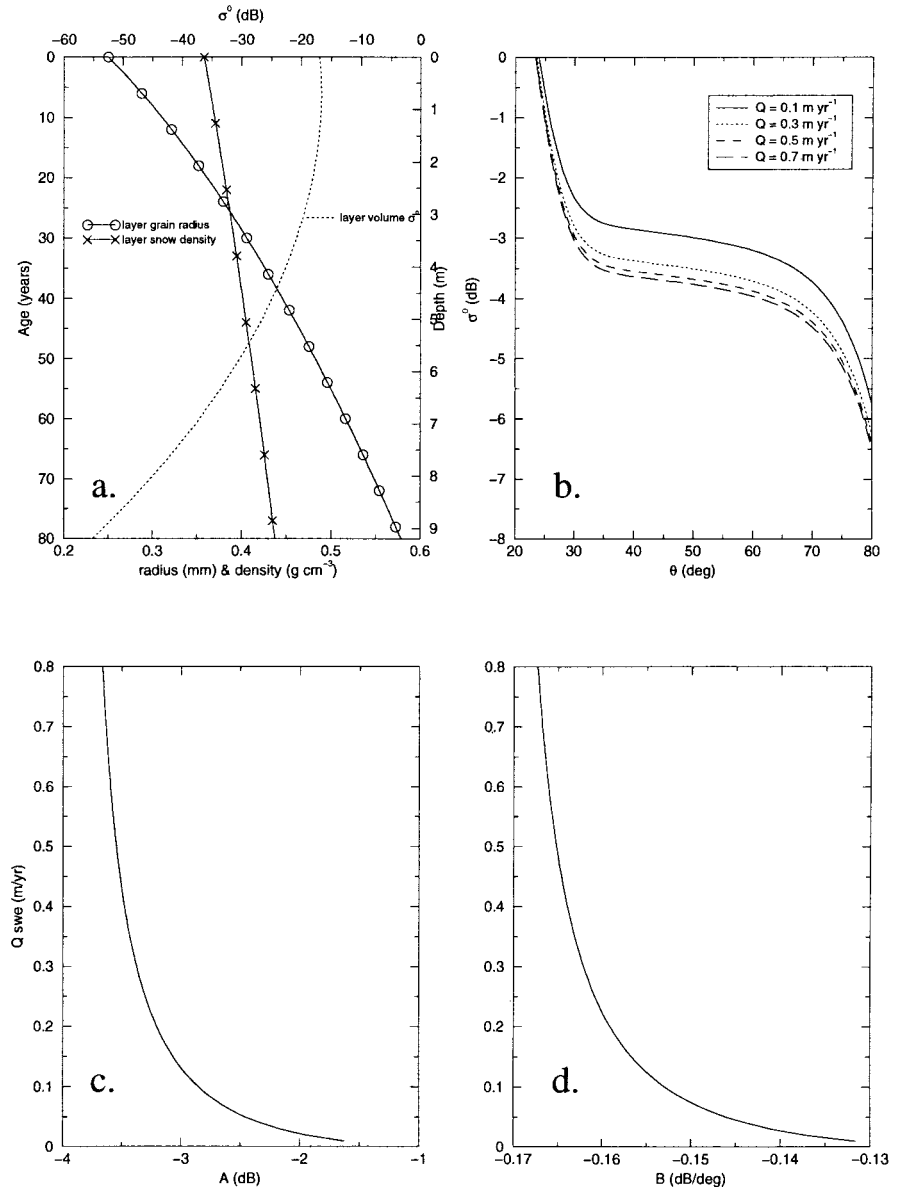

Figure 3. Modeled Ku band A and B values as a function of layered firn characteristics. (a) Depth profiles of layer grain radius (circles), firn density (crosses), and depth-dependent volume scattering coefficient (dotted line). (b) Angular backscatter response from layered firn with variable accumulation Q at 0.2 m yr^{-1} intervals from 0.1 to 0.7 m yr^{-1} SWE. (c) Modeled relationship between A and Q. (d) Modeled relationship between B and Q.

dry snow zone, a solid black line is used to indicate the dry snow line. This allows the spatial gradients in retrieved Q values around the margins to be observed. A color legend and contours at 0.20 m and 0.30 m are used to indicate the broad spatial variability in Q. Camp Century and Summit reference points are shown (stars) and indicate close agreement with the retrieved Q values. The lowest estimates of Q are found in northern Greenland to the northeast of the crestline of the ice sheet. The largest estimates of Q (>0.70 m yr^{-1}) are obtained along the southeastern flank of the dry snow zone.

5.2. Validation of Snow Accumulation Retrievals

A validation line is selected in Plate 4 that corresponds with the snow accumulation transect defined by *Dahl-Jensen et al.* [1997]. This transect follows a line along the ice sheet crest between a point at the Greenland Ice Core Project (GRIP) (72.6°N, 37.62°W) near the ice sheet summit (3232-m elevation) and a point 500 km to the north-northwest. The transect follows the series of pits 5-0 through 4-0 studied by *Benson* [1962] and passes through the location of the European North Greenland Ice Core Project (NGRIP) drill site (75.12°N, 42.35°W, 2919 m elevation). NSCAT accumulation estimates extracted along this line are shown in Figure 4 as a dashed line (together with a 1σ error bar derived from analysis of the residuals in the Figure 2 relationship). Comparative accumulation rates shown in Figure 4 are derived from the snow pit data of Benson and from volcanic isochrones identified as stratigraphic markers in echo sounding and in the NGRIP ice core data [*Dahl-Jensen et al.*, 1997].

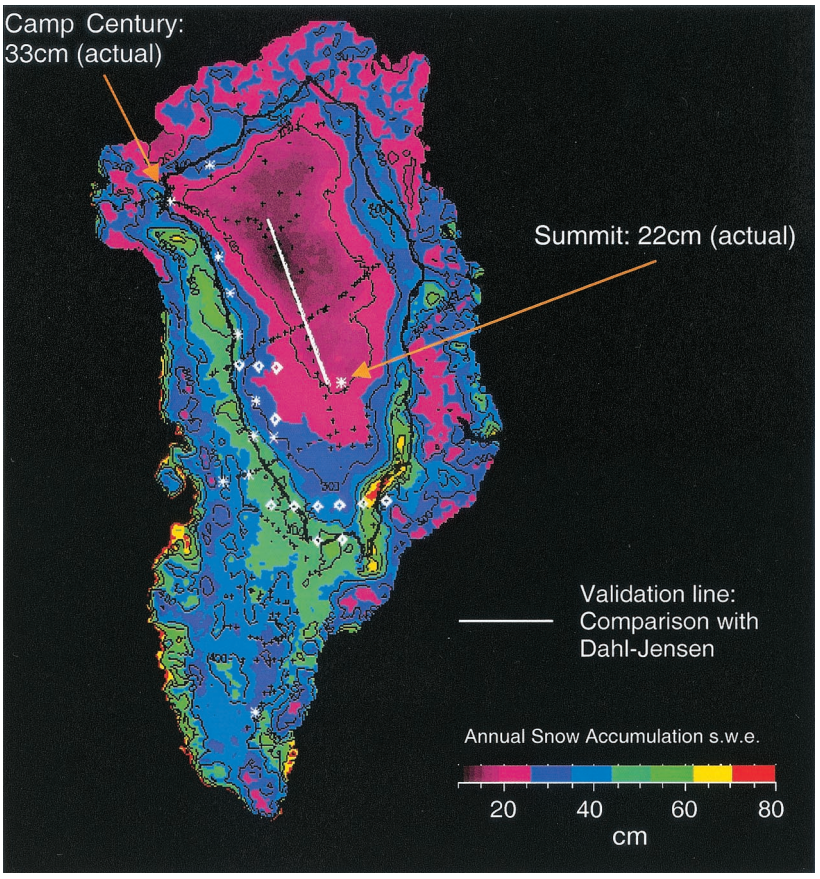

Plate 4. Predicted snow accumulation from NSCAT *B* values, using the exponential relationship in Figure 2. Stars indicate sites shown in Plates 2 and 3, and other symbols indicate recent PARCA in situ data sites. Note that accumulation estimates are only valid within the dry snow line (indicated by the solid black line derived from Plate 2).

At the beginning of the transect our data correspond fairly closely with a number of shallow core accumulation rates reported by *Bolzan and Stroebel* [1994] near the ice sheet summit. These data indicate annual accumulation values between 0.18 and 0.28 m SWE, and thus the NSCAT retrieval in this location is representative of the long-term mean accumulation. NSCAT estimates decrease at a similar rate to the in situ measurement data toward the northwest. A small secondary peak in the transect at around 275 km matches closely the occurrence of a small peak in the in situ data, albeit smaller in magnitude. This peak occurs at the location where the Koch-Wegener and Benson snow pit lines intersect in the *Ohmura and Reeh* [1991] accumulation maps (at around 74°12′N, 42°2′W). In this location, *Benson* [1962] reports differences between the Koch-Wegener data and his own snow pit data of 0.17 versus 0.23 m SWE. The intrinsic difference in period and time interval captured by these snow pit data appears to be responsible for this inconsistency. The small discrepancy between the in situ and NSCAT estimates between 240 and 290 km is not surprising given that the crestline accumulation exhibits significant interannual variability of the order of size of the 1σ error bar in Figure 4. From 300 to 450 km distance the annual snow accumulation rate drops to its lowest values, below 0.17 m yr^{-1} SWE.

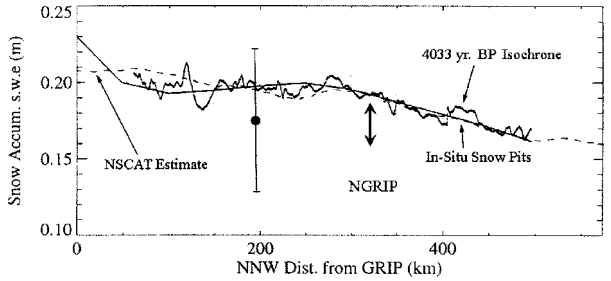

Figure 4. Comparison of NSCAT accumulation retrieval (dashed line) from days 261 to 266, 1996, along the validation line in Figure 3. *Dahl-Jensen et al.* [1997] volcanic isochrone-inferred accumulation (thick solid line) and in situ shallow core and snow pit data (thin solid line) [after *Clausen et al.*, 1988; *Ohmura and Reeh*, 1991; *Bolzan and Stroebel*, 1994] are shown for comparison.

Benson's [1962] snow pit accumulation values and the shallow core values are representative of the mean of many annual layers of accumulation. Figure 4 appears to indicate that the ice sheet presents significant topographic controls on snow accumulation that are expressed interannually as spatial differences in accumulation. Figure 4 shows that the contemporary 1996 snow accumulation picture is consistent with the general accumulation trend along the north-northwest trending ridge, with some characteristics common to the long-term mean pattern. The summit contains extremely accurate accu-

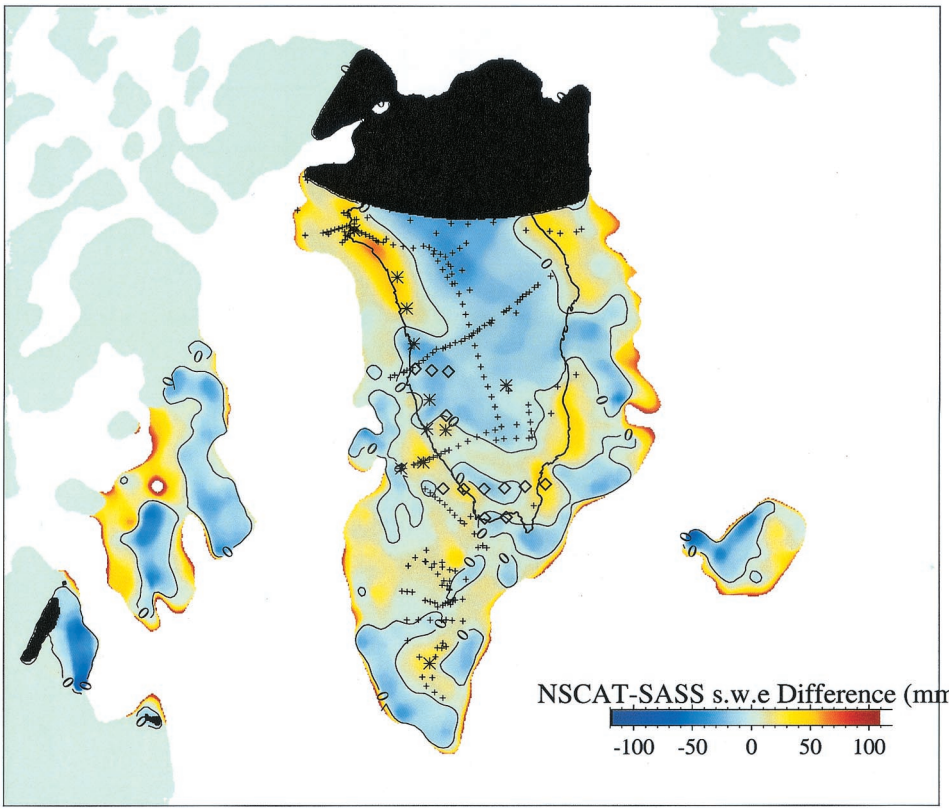

Plate 5. Difference of Ku band NSCAT and Seasat SASS snow accumulation retrieval estimates using an identical empirical relationship. Blue indicates reductions, and red indicates increases in accumulation over the 18-year interval 1978–1996. Values close to zero reflect stable net balance over the last 2 decades. Crosses and diamonds represent in situ measurement locations. Note that accumulation estimates are only valid within the dry snow zone (contained within the thick black contour derived from Plate 2).

mulation estimates, which *Bolzan and Stroebel* [1994] weight by the most recent accumulation values. Further, their results indicate that the summit of the ice sheet is in steady state (i.e., contemporary snow accumulation is consistent with the mean derived from the last 4000 years record of *Dahl-Jensen et al.* [1997]). It is not surprising therefore that all three data sets are quite consistent in this location.

5.3. 1978–1996 Estimated Accumulation Changes

Estimates of short-term changes in snow accumulation are made by computing differences between Seasat and NSCAT accumulation predictions from their respective B values (using the relationship in Figure 2). The assumption is made that the radar integrates over the top layers of the firn and that changes in the seasonality in precipitation in the most recent year do not adversely impact the result. Plate 5 shows the difference between Ku band NSCAT and SASS mean snow accumulation estimates, each made from SIR images from an identical 2-week period in late September. Valid estimates are contained within the thick black line encompassing the dry snow zone. Values range from increases exceeding $+0.05$ m yr^{-1} SWE in the location of GITS (Camp Century) to decreases of the order of 0.05 m yr^{-1} SWE in north central Greenland. The zero contour delineates the positive and negative regimes.

As described in section 3, the estimation accuracy is of the order of 0.05 m yr^{-1} and so the most significant changes are observed on the northwestern flank of the ice sheet near Camp Century (GITS). This strong positive accumulation trend is confined to the southwest of the crest and is consistent with in situ observations of an increasing trend from 76°N, 53°W northward to GITS [*Mosley-Thompson et al.*, this issue]. The positive trend changes sign south of ~74.5°N and is also consistent with a switch noted by *Mosley-Thompson et al.* [this issue] from a strong positive to a modest decreasing trend in accumulation along a transect between the shallow core site at 75°N, 51°W and NASA-U. At latitudes exceeding 76°N, east of the central Greenland ice divide, the accumulation trend is significant and predominantly negative (<0.05 m yr^{-1}). The majority of the remainder of the central dry snow zone indicates values not statistically significantly different from zero. Estimates south and east of the summit show a reversal back to a positive trend along the southeastern flank of the dry snow zone (between 69° and 70°N). Values close to 0.05 m yr^{-1} are not inconsistent with Geosat-Seasat height differences observed by *Davis et al.* [2000] during the earlier half (1978–1988) of the interval or with laser measurements by *Krabill et al.* [1995] during the period from 1980 to 1993–1994.

5.4. Recent Changes

Data from the Ku band SeaWinds scatterometer aboard the ongoing QSCAT satellite mission allow comparisons to be made with the NSCAT and SASS data. This permits analysis of the most recent changes in ice sheet surface characteristics. Since SeaWinds is not a fan-beam scatterometer, it does not facilitate direct characterization of B using (1). Until a scheme

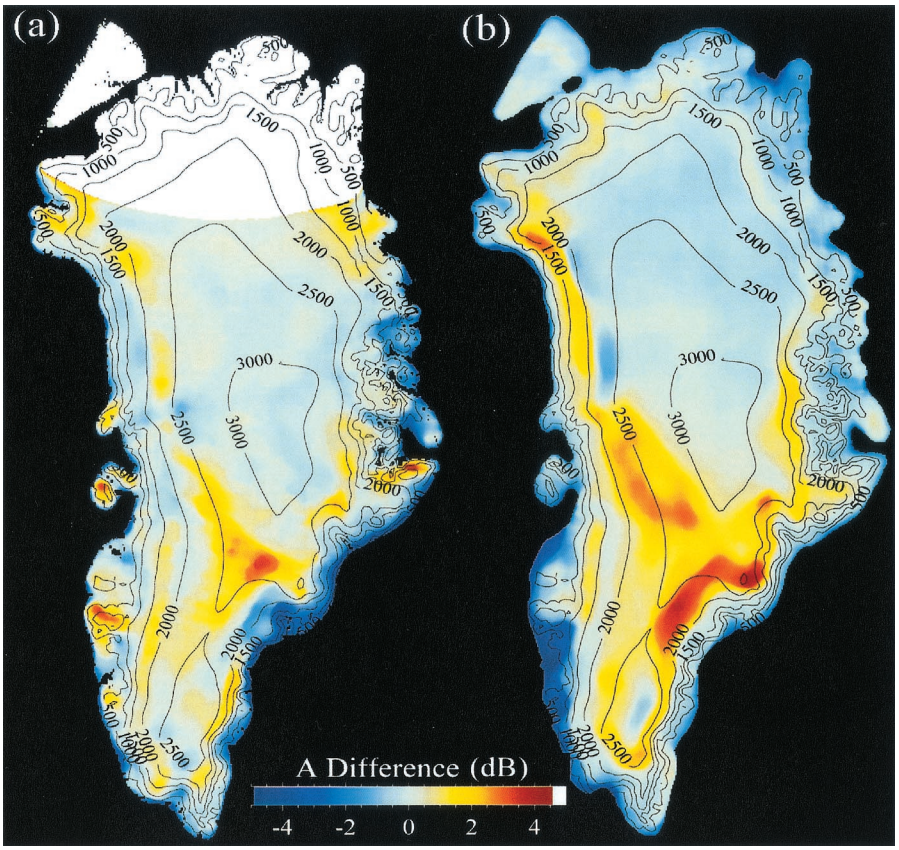

Plate 6. Comparison of Ku band A difference images for (a) NSCAT − SASS (1996 − 1978) for the seasonal period spanning days 267–272 and (b) QSCAT − NSCAT (2000 − 1997) for the seasonal period spanning days 21–26. Contours indicate ice sheet elevations (in meters) derived from the digital terrain model of *Bamber et al*. [2001].

can be devised to measure polarization-corrected differences between the single, fixed HH polarization 46° and VV polarization 54° beams, estimation of Q is not possible using a semiempirical relationship such as (3). Instead, Plate 6 shows a comparison of the VV polarization ΔA difference images for NSCAT − SASS (1996 − 1978) and QSCAT − NSCAT (2000 − 1997), with identical scaling. As QSCAT VV polarization A data are from a fixed measurement incidence angle of 54° (rather than 40°), we first corrected NSCAT σ° data to 54° by inserting A, B, and $\theta = 54°$ in (1). The resulting QSCAT − NSCAT A difference image is shown in Plate 6b at this higher incidence angle. Although a 14° incidence angle offset implies a reduction in absolute terms of −1 to −2 dB in each image, the difference in Plate 6b is largely independent of incidence angle.

Significant reversals in differences are still apparent between 1997 and 2000 in many regions. The most obvious example is the apparent transition from positive to negative ΔA values along the northwestern flank of the Greenland ice sheet between 2000 and 2500 m elevation, particularly north of 70°N latitude. A change from positive to negative ΔA implies a net reduction in σ°, which at high incidence angles suggests an increase in layer thickness or an increase in Q (see Figure 3). Reductions of −1 dB or more are observed to accompany increases in Q of 0.10 m yr^{-1} in regions where percolation features have formerly been observed. The progressive burial of what were originally shallow ice lenses and glands is thought to be responsible for the disappearance of the regions of strong positive ΔA values in Plate 6a. New small positive ΔA values are also evident at lower elevations at the same latitudes (in contrast to Plate 6a). These areas indicate a winter increase in ΔA of up to 2 dB, providing evidence for the growth of percolation features by lower-elevation summer surface melting over the corresponding time interval.

Most dramatic are the large increases in extent of positive A difference values over the recent 3-year interval (Plate 6b). Significant increases in A values around the periphery of the dry snow zone signify an increase in scattering from internal inhomogeneities produced by melting. Despite the cautionary note that interannual variability can have significant impact on the intensity and spatial extent of melting, it is clear that microwaves integrate over depth-equivalent decades of dry snow accumulation. The latter implies that ice lenses formed in the recent past (perhaps produced during extreme melt anomalies) have a persistent effect upon high-incidence microwave radar scatterometer images. Thus increasing spatial extent in positive differences in A between one year and the next would appear to provide irrefutable evidence of the cumulative effects of melting. Plate 6a shows an 18-year difference while Plate 6b shows dramatic evidence of accelerated changes over the much shorter 3-year interval between NSCAT and QSCAT (2000 and 1997, respectively). This increase in recent years charts the spatial extent in melting thought to be responsible for the rapid thinning of the periphery of the Greenland ice sheet observed in airborne laser profile data [*Abdalati et al*., this issue; *Krabill et al*., 2000]. Our data indicate not only the

effects around the periphery but also the increased spatial extent of ablation at higher elevations on the southwestern flank of the ice cap.

Reversals in what appear to have been stable trends in Plate 6a may indicate large-scale changes in precipitation and ablation patterns, particularly along the western flank of the ice sheet. Short-term changes are consistent with previous indications of strong variability in net accumulation in the NASA-U core [*Anklin et al*., 1998; *Appenzeller et al*., 1998]. Since summer-fall precipitation and summer ablation in northwestern Greenland are regulated by the strength of cyclonic activity over Baffin Bay, changes observed here may indicate a reorganization in large-scale atmospheric circulation. Recalling that net precipitation is reduced over western Greenland during positive phases of the North Atlantic Oscillation (NAO), a change in summer and autumn phase of the NAO (as defined by *Hurrell* [1995]) may imply a reduction in summer cyclonic activity in the Icelandic low region and a tendency toward more winter storms originating in Davis Strait. Subsequent results from QSCAT should be investigated to confirm such trends and to assess the impact which these changes have had on accumulation in the dry snow zone.

6. Conclusions

Results presented in this paper demonstrate that microwave radar scatterometer images from SASS, EScat, NSCAT, and QSCAT provide an extremely powerful tool for investigating changes in the characteristics of the Greenland ice sheet in relation to climate changes over the last 2 decades. The advantages of the scatterometer over higher-resolution synthetic aperture radar are its frequent, high incidence angle coverage of the entire ice sheet and the fact that it provides the longest continuous record of microwave radar backscatter. Furthermore, SIR enhanced resolution data processing yields images comparable in spatial resolution and pixel spacing to passive microwave data and comparable in coverage to recent ice sheet mosaics developed from individual high-resolution SAR images.

We exploited overlapping VV Ku and C band data sets (from NSCAT and EScat, respectively) to define the seasonally varying response of the percolation zone in order to demarcate the dry snow line. Our results are confined to the common operating period of each of the scatterometers and focus on the fall-winter microwave response of the dry snow facies. During this season, σ° (at an incidence angle of 40°) varies little over time, and the gradient in σ° (or B) is sensitive to the mean snow accumulation over the last several years. Late September NSCAT results were used to develop empirical relationships used for making Ku band accumulation estimates. The implication for this seasonally specific algorithm is that by early winter the seasonal cold temperature wave has penetrated sufficiently deeply to allow the radar to penetrate and integrate over the top surface layers of firn. Indeed, the thermal profile may help to confine the scattering response to the most recent upper layers of accumulated firn in late September and early October, thereby accounting for the strength of the observed correlation. In the future, multiple years of Ku band data will allow development of seasonally adjusted accumulation retrieval algorithms.

The difficulty in establishing accumulation trends from single shallow cores highlights the need for a satellite retrieval method that provides a realistic picture of the spatial variations. Annual accumulation rates derived from ice cores show interannual variability due to precipitation variability as well as roughness effects such as sastrugi and topographically induced accumulation variability. Large differences are evident between different local shallow core and snow pit annual accumulation values, making it difficult to derive an accurate representation of recent accumulation rate. Here we observe that a Ku band scatterometer integrates and averages over the top layers of dry snow. The imaging method effectively results in a low-pass spatially filtered image of B variations, and inversion of the simple empirical algorithm provides a relatively smooth accumulation field with variability at the 5–20 km scale (depending on the satellite data used). The technique is reasonably robust when compared with all available historical data, indicating an RMS error of 0.05 in SWE of the order of observed interannual accumulation variations. Comparisons made along a transect in a steady state region of the dry snow zone also indicate close correspondence between satellite estimates and in situ measurements.

Results of applying the simple empirical relation yield accumulation differences that indicate changes in the spatial patterns of Greenland snow accumulation and melting during the intervals 1978–1996 and 1997–2000. Observed changes are interpreted as a recent large-scale reversal in the net accumulation trends along large parts of the northwestern flank of Greenland that indicate more frequent cyclonic activity in Baffin Bay and in turn more frequent negative phases of the NAO. These results warrant a more detailed investigation as more extensive time series data are acquired by QSCAT.

A future objective is to be able to acquire daily global coverage of high-latitude snow and ice surfaces in a combined, active-passive satellite microwave data set. In order to obtain sufficient coverage the instrument requirement is for a swath of a minimum of 500 km width. The instrument should make simultaneous overlapping active and passive swath measurements of equivalent swath width, with global coverage achieved within 24 hours. ADEOS-II data will meet many of these requirements, providing temporally and spatially collocated Advanced Microwave Scanning Radiometer multichannel radiometer and Ku band SeaWinds-II scatterometer data. This presents an opportunity to develop future multifrequency, multipolarization algorithms for routine extraction of snow accumulation.

Acknowledgments. Preben Gudmandsen is acknowledged for his ideas and inspiration to further investigate the applicability of scatterometer data to snow accumulation retrieval. NSCAT data were obtained from the PO.DAAC at the Jet Propulsion Laboratory, and ERS-1 and ERS-2 scatterometer data were processed as part of ESA study AO2.USA.119. This work was partly performed by M.R.D. at the Jet Propulsion Laboratory, California Institute of Technology, under contract to the National Aeronautics and Space Administration. Support was provided for M.R.D. and D.G.L. through the NASA Scatterometer Climate Record Pathfinder Project and JPL NASA grant 621-82-80. A.W.B. was supported by a National Research Council Resident Research Associateship Award.

References

Abdalati, W., and K. Steffen, Snowmelt on the Greenland ice sheet as derived from passive microwave satellite data, *J. Clim*., *10*(2), 165–175, 1997.

Abdalati, W., W. Krabill, E. Frederick, S. Manizade, C. Martin, J. Sonntag, R. Swift, R. Thomas, W. Wright, and J. Yungel, Outlet glacier and margin elevation changes: Near-coastal thinning of the Greenland ice sheet, *J. Geophys. Res*., this issue.

Alley, R. B., J. F. Bolzan, and I. M. Whillans, Polar firn densification and grain growth, *Ann. Glaciol.*, *3*, 7–11, 1982.

Anklin, M., R. C. Bales, E. Mosley-Thompson, and J. McConnell, Annual accumulation at two sites in northwest Greenland during recent centuries, *J. Geophys. Res.*, *103*(D22), 28,775–28,783, 1998.

Appenzeller, C., T. F. Stocker, and M. Anklin, North Atlantic oscillation dynamics recorded in Greenland ice cores, *Science*, *282*, 446–449, 1998.

Attema, E. P. W., and F. T. Ulaby, Vegetation modeled as a water cloud, *Radio Sci.*, *13*, 357–364, 1978.

Bales, R. C., J. R. McConnell, E. Mosley-Thompson, and G. Lamorey, Accumulation map for the Greenland ice sheet: 1971–1990, *Geophys. Res. Lett.*, *28*(15), 2967–2970, 2001.

Bamber, J. L., S. Ekholm, and W. B. Krabill, A new, high-resolution digital elevation model of Greenland fully validated with airborne laser altimeter data, *J. Geophys. Res.*, *106*(D4), 6733–6745, 2001.

Barlow, L. K., J. C. Rogers, M. C. Serreze, and R. G. Barry, Aspects of climate variability in the North Atlantic sector: Discussion and relation to the Greenland Ice Sheet Project 2 high-resolution isotopic signal, *J. Geophys. Res.*, *102*(C12), 26,333–26,344, 1997.

Benson, C. S., Stratigraphic studies in the snow and firn of the Greenland ice sheet, *CRREL Res. Rep. 70*, 120 pp., Cold Reg. Res. and Eng. Lab., Hanover, N. H., 1962.

Bingham, A. W., Monitoring arctic glaciers and ice caps using satellite remote sensing, Ph.D. thesis, Univ. of Cambridge, Cambridge, England, 1997.

Bingham, A. W., and M. Drinkwater, Recent changes in the microwave scattering properties of the Antarctic ice sheet, *IEEE Trans. Geosci. Remote Sens.*, *38*(4), 1810–1820, 2000.

Bolzan, J. F., Ice flow at the Dome C ice divide based on a deep temperature profile, *J. Geophys. Res.*, *90*(D5), 8111–8214, 1985.

Bolzan, J. F., and M. Stroebel, Accumulation rate variations around Summit, Greenland, *J. Glaciol.*, *40*, 56–66, 1994.

Clausen, H. B., N. S. Gunderstrup, S. J. Johnsen, R. Bindschadler, and H. J. Zwally, Glaciological investigations in the Crete area, central Greenland: A search for a new deep drilling site, *Ann. Glaciol.*, *10*, 10–15, 1988.

Comiso, J. C., H. J. Zwally, and J. L. Saba, Radiative transfer modeling of microwave emission and dependence on firn properties, *Ann. Glaciol.*, *3*, 54–58, 1982.

Cuffey, K. M., and G. D. Clow, Temperature, accumulation, and ice sheet elevation in central Greenland through the last glacial transition, *J. Geophys. Res.*, *102*(C12), 26,383–26,396, 1997.

Dahl-Jensen, D., N. S. Gunderstrup, K. Keller, S. J. Johnsen, S. P. Gogineni, C. T. Allen, T. S. Chuah, H. Miller, S. Kipfstuhl, and E. D. Waddington, A search in north Greenland for a new ice-core drill site, *J. Glaciol.*, *43*, 300–306, 1997.

Davis, C. H., C. A. Kluever, and B. J. Haines, Elevation change of the southern Greenland ice sheet, *Science*, *27*, 2086–2088, 1998.

Davis, C. H., C. A. Kluever, B. J. Haines, C. Perez, and Y. Yoon, Improved elevation change measurement of the southern Greenland ice sheet from satellite radar altimetry, *IEEE Trans. Geosci. Remote Sens.*, *38*(3), 1367–1378, 2000.

Drinkwater, M. R., and D. G. Long, Seasat, ERS-1/2 and NSCAT scatterometer-observed changes on the large ice sheets, *Eur. Space Agency Spec. Publ.*, *ESA SP-424*, 91–96, 1998.

Drinkwater, M. R., D. G. Long, and D. S. Early, Enhanced resolution scatterometer imaging of Southern Ocean sea ice, *Eur. Space Agency J.*, *17*, 307–322, 1993.

Eom, H. J., Theoretical scatter and emission models for microwave remote sensing, Ph.D. dissertation, Univ. of Kansas, Lawrence, Kansas, 1982.

Fahnestock, M., R. Bindschadler, R. Kwok, and K. Jezek, Greenland ice-sheet surface properties and ice dynamics from ERS-1 SAR imagery, *Science*, *262*, 1530–1534, 1993.

Forster, R., K. C. Jezek, J. Bolzan, F. Baumgartner, and S. P. Gogineni, Relationships between radar backscatter and accumulation rates on the Greenland ice sheet, *Int. J. Remote Sens.*, *20*(15/16), 3131–3147, 1999.

Gow, A. J., Deep core studies of the accumulation and densification of snow at Byrd Station and Little America V, Antarctica, *CRREL Res. Rep. 197*, *197*, Cold Reg. Res. and Eng. Lab., Hanover, N. H., 1968.

Gow, A. J., On the rates of growth of grains and crystals in south polar firn, *J. Glaciol.*, *8*, 241–252, 1969.

Hurrell, J. W., Decadal trends in the North Atlantic Oscillation and relationships to regional temperature and precipitation, *Science*, *269*, 676–679, 1995.

Jezek, K. C., M. R. Drinkwater, J. P. Crawford, R. Bindschadler, and R. Kwok, Analysis of synthetic aperture radar data collected over the southwestern Greenland ice sheet, *J. Glaciol.*, *39*, 131, 119–132, 1993.

Jezek, K. C., P. Gogineni, and M. Shanableh, Radar measurements of melt zones on the Greenland ice sheet, *Geophys. Res. Lett.*, *21*(1), 33–36, 1994.

Joughin, I. R., D. P. Winebrenner, and M. A. Fahnestock, Observations of ice sheet motion in Greenland using satellite radar interferometry, *Geophys. Res. Lett.*, *22*(5), 571–574, 1995.

Krabill, W., R. Thomas, K. Jezek, K. Kuivinen, and S. Manizade, Greenland ice sheet thickness changes measured by laser altimetry, *Geophys. Res. Lett.*, *22*(17), 2341–2344, 1995.

Krabill, W., W. Abdalati, E. Frederick, S. Manizade, C. Martin, J. Sonntag, R. Swift, R. Thomas, W. Wright, and J. Yungel, Greenland ice sheet: High-elevation balance and peripheral thinning, *Science*, *289*, 428–430, 2000.

Kruopis, N., Microwave remote sensing of snow cover, Ph.D. thesis, Kaunas Univ. of Technol., Kaunas, Lithuania, 1999.

Long, D. G., and M. R. Drinkwater, Greenland ice-sheet surface properties observed by the Seasat-A scatterometer at enhanced resolution, *J. Glaciol.*, *40*, 213–230, 1994.

Long, D. G., and M. R. Drinkwater, Cryosphere applications of NSCAT data, *IEEE Trans. Geosci. Remote Sens.*, *37*(3), 1671–1684, 1999.

Long, D. G., and M. R. Drinkwater, Azimuth variation in microwave scatterometer and radiometer data over Antarctica, *IEEE Trans. Geosci. Remote Sens.*, *38*(4), 1857–1870, 2000.

Long, D. G., and G. B. Skouson, Calibration of spaceborne scatterometers using tropical rain forests, *IEEE Trans. Geosci. Remote Sens.*, *34*(2), 413–424, 1996.

Long, D. G., P. J. Hardin, and P. T. Whiting, Resolution enhancement of spaceborne scatterometer data, *IEEE Trans. Geosci. Remote Sens.*, *31*(3), 700–715, 1993.

Mätzler, C., Applications of the interaction of microwaves with the natural snow cover, *Remote Sens. Rev.*, *2*, 259–392, 1987.

Mosley-Thompson, E. S., J. R. McConnell, R. C. Bales, Z. Li, P.-N. Lin, K. Steffen, L. G. Thompson, R. Edwards, and D. Bathke, Local to regional-scale variability of annual net accumulation on the Greenland ice sheet from PARCA cores, *J. Geophys. Res.*, this issue.

Mote, T. L., and M. R. Anderson, Variations in snowpack melt on the Greenland ice sheet based on passive microwave measurements, *J. Glaciol.*, *41*, 51–60, 1995.

Naderi, F., M. H. Freilich, and D. G. Long, Spaceborne radar measurement of wind velocity over the ocean—An overview of the NSCAT scatterometer system, *Proc. IEEE*, *79*(6), 850–866, 1991.

Ohmura, A., and N. Reeh, New precipitation and accumulation maps for Greenland, *J. Glaciol.*, *37*, 140–148, 1991.

Paterson, W. S., *The Physics of Glaciers*, Pergamon, New York, 1994.

Rott, H., Synthetic aperture radar capabilities for glacier monitoring demonstrated with Seasat SAR data, *Z. Gletscherk. Glazialgeol.*, *16*, 255–266, 1980.

Shuman, C. A., R. B. Alley, M. A. Fahnestock, R. A. Bindschadler, J. W. C. White, J. R. McConnell, and J. Winterle, Temperature history and accumulation timing for the snow pack at GISP2, central Greenland, *J. Glaciol.*, *44*, 21–30, 1998.

Shuman, C. A., D. H. Bromwich, J. Kipfstuhl, and M. Schwager, Multiyear accumulation and temperature history near the North Greenland Ice Core Project site, north central Greenland, *J. Geophys. Res.*, this issue.

Spencer, M. W., C. Wu, and D. G. Long, Tradeoffs in the design of a spaceborne scanning pencil-beam scatterometer, *IEEE Trans. Geosci. Remote Sens.*, *35*(1), 115–126, 1997.

Spencer, M. W., C. Wu, and D. G. Long, Improved resolution backscatter measurements with the SeaWinds pencil-beam scatterometer, *IEEE Trans. Geosci. Remote Sens.*, *38*(1), 89–104, 2000.

Thomas, R. H., R. A. Bindschadler, R. L. Cameron, F. D. Carsey, B. Holt, T. J. Hughes, C. W. M. Swithinbank, I. M. Williams, and H. J. Zwally, Satellite remote sensing for ice sheet research, *NASA Tech. Memo.*, *TM-86233*, 32, 1985.

Thomas, R. H., T. Akins, B. Csatho, M. Fahnestock, S. P. Gogineni, C. Kim, and J. Sonntag, Mass balance of the Greenland ice sheet at high elevations, *Science*, *289*, 426–427, 2000.

Ulaby, F. T., R. K. Moore, and A. K. Fung, *Microwave Remote Sensing:*

Active and Passive, vol. II, *Radar Remote Sensing and Surface Scattering and Emission Theory*, Addison-Wesley, Reading, Mass., 1982.

Wismann, V. R., Monitoring of seasonal snowmelt in Greenland with ERS scatterometer data, *IEEE Trans. Geosci. Remote Sens.*, *38*(4), 1821–1826, 2000.

Wismann, V. R., and K. Boehnke, Dramatic decrease in radar cross section over Greenland observed by the ERS-1 scatterometer between 1991 and 1995, paper presented at IGARSS '96 Inst. of Electr. and Electron. Eng., Lincoln, Nebr., 1996.

Wismann, V. R., and K. Boehnke, Monitoring snow properties on Greenland with ERS scatterometer and SAR, *Eur. Space Agency Spec. Publ.*, *ESA SP-414*, 857–862, 1997.

Zwally, H. J., Microwave emissivity and accumulation rate of polar firn, *J. Glaciol.*, *18*, 195–215, 1977.

Zwally, H. J., and A. C. Brenner, Growth of the Greenland ice sheet, *Science*, *246*, 1587–1591, 1989.

Zwally, H. J., and M. B. Giovinetto, Accumulation in Antarctica and Greenland derived from passive-microwave data: A comparison with contoured compilations, *Ann. Glaciol.*, *21*, 123–130, 1995.

A. W. Bingham, Jet Propulsion Laboratory, California Institute of Technology, 4800 Oak Grove Drive, Pasadena, CA 91109. (andrew.bingham@jpl.nasa.gov)

M. R. Drinkwater, Earth Sciences Division, European Space Agency, Keplerlaan 1, Postbus 299, NL 2200 AG Noordwijk ZH, Netherlands. (mark.drinkwater@esa.int)

D. G. Long, Microwave Remote Sensing Laboratory, Brigham Young University, 459 Clyde Building, Provo, UT 84602. (long@ee.byu.edu)

(Received August 3, 2000; revised January 23, 2001;
accepted January 30, 2001.)